GEOFFREY B. IRANI and BRUCE L. GOTWOLS

WAVDYN: MEASUREMENTS OF THE INDEPENDENCE OF OCEAN WIND WAVES

The Ocean Wave Dynamics Experiment (WAVDYN), an empirical investigation of ocean wind waves in deep open water, has yielded improved evidence that independently (freely) propagating waves prevail over manifestations of their nonsinusoidal (nonlinear) waveforms. Measurements were made during September 1978 with an array of surface elevation transducers, a two-axis current meter, and a video-based wave-imaging system deployed at an ocean tower.

INTRODUCTION

Wind waves traveling across a water surface form patterns that catch the eye and interest of most of us. When the wind blows steadily over a small body of water, we see a pattern of waves that appears quite regular. On large bodies of water when the wind is strong, we need a high vantage point, such as an airplane, to perceive the wave pattern, which then appears much like the wave pattern on a pond. From experience, sailors know that, as the expanse of water over which a strong wind blows (the fetch) increases, the main waves get steeper and longer, sometimes steepening to the point of breaking even in deep water. Shorter and less regular waves, ranging down to very small scales, are scattered among the main (dominant) waves. Such observations are clues that a wind-driven surface is a complex composite of moving waves. Yet waves on a pond or on an ocean possess a substantial degree of regularity, and their characteristics, which are dictated by the physics of their formation and propagation, must be similar. Since the restoring force of gravity is essentially constant, wind speed and fetch must be the primary differentiating factors in deep water where the bottom does not substantially influence wave propagation. Gravity waves are briefly described in Ref. 1.

The development of models predicting wind-wave behavior is a goal for basic research and is also required for a number of practical applications. Probably the most obvious application is forecasting storm waves so that ships can be routed for safety and efficiency. Other applications include ship design, beach erosion, and ocean resources development. Perhaps a less obvious application is the interpretation of data from remote sensors — for example, locating eddy currents through their modification of wind waves that, in turn, modulate the signal of a remote sensor. Such currents influence the level of nutrients and biological activity and indicate potential concentrations of fish.

The development of usefully accurate descriptions of wind waves is not an easy task. Physical oceanographers explain wind-wave behavior by using a combination of deterministic and statistical relations. Physics enters deterministically, while the complexity of numerous waves traveling in various directions and with various phase relationships is treated statistically. Over a limited area of the sea, oceanographers imagine wind waves to be represented by independent (free) wave trains, each having a unique amplitude, wave number, propagation direction, and frequency. Each wave train can be represented mathematically as a fundamental sinusoidal wave plus other sinusoids, including harmonics of the fundamental that account for its asymmetry and its limited extent (group length). These sinusoidal waves constitute the components of a wind-wave spectrum. Such spectra commonly represent the variance of sea surface elevation, slope, or curvature. Phase relationships between the components that represent free waves are random, whereas phase relationships between harmonic components and their fundamental wave are fixed. Thus, the harmonics are called bound waves; they are nondispersive.

In their general form, the hydrodynamic equations for water waves are intractably complex. Therefore, various approximations are used that reduce them to tractable forms while preserving (it is hoped) the salient characteristics of the physics. Most formalism describing wind waves uses either linear or weakly nonlinear equations to describe wave dynamics. The linear equations exclude harmonics and any interactions between spectral components. Each component travels at a different rate, characterized by its frequency and its wave number, and thus represents a dispersive wave. The weakly nonlinear equations, a step away from the simplest theory, permit gradual exchange of energy and momentum between spectral components in order to explain the excitation of waves by wind and the increase, or growth, of the amplitudes of long-wave components. Nonlinearity of the wave trains means that their spectral representation includes harmonics and sidebands in addition to the fundamental wave.

As noted, wind-wave spectra represent the distributions of surface elevation, slope, or curvature variance over a three-dimensional space that measures

the direction of wave propagation α, the wave number k (inverse wavelength), and the frequency f. In this directional wave-number/frequency space, Fig. 1 depicts theoretical relationships between wave number and frequency for sinusoidal waves (the paraboloid) and for harmonics of the dominant wave (the dashed line). Parameters describing the dominant wave carry the subscript d. If displacements of an unbounded water surface from its mean level resulted only from free sinusoidal waves, the spectral density would be nonzero only on the paraboloid. Departures from this idealization require finite spectral density at points that are not on this surface. Since the dominant wave causes most of the surface-elevation variance, its harmonics represent the most important departures from linear theory. These harmonics propagate in the same direction as the dominant wave and therefore lie in the plane outlined in blue in Fig. 1.

In recent years, research performed in several countries and based primarily on laboratory measurements has indicated that strongly nonlinear waves — waves with very steep slopes — have substantially more complex dynamics and stronger exchanges of energy between spectral components than nearly linear waves have.[2-5] Such strong nonlinearity counters the randomness of turbulent generation processes and can lead to a single, largely coherent wave train that undergoes amplitude and frequency modulations as it propagates. Its temporal spectrum appears much like modeled wind-wave spectra with the addition of some strong components, but its components are nondispersive, being phase-locked, or bound, to the peak (dominant) component.

This situation sharply contrasts with the classical assumption that wind waves are the incoherent superposition of many near-linear wave trains. The implications of this controversy are both interesting and important: The vast majority of wave research and modeling is based on linear and near-linear theory, which could be misleading.

Stimulated by the impact of the nonlinear model on the validity of predictions of ocean wave evolution and by the lack of relevant experimental evidence, APL undertook an experimental investigation of ocean waves. This effort, called the Ocean Wave Dynamics Experiment (WAVDYN), measured the phase speeds of spectral components in the short-to-moderate gravity wave regime (wavelengths between 20 centimeters and 30 meters). The objective was to acquire evidence on the prominence of bound waves relative to free waves in ocean wind-wave systems as manifested in estimates of their directional wave-number/frequency spectra. A brief description of the experiment and preliminary video results appeared in an earlier issue of this journal.[1]

THE MEASUREMENTS

Briefly stated, the scheme for meeting this objective involved recording variations in surface elevation and radiance together with current and wind mea-
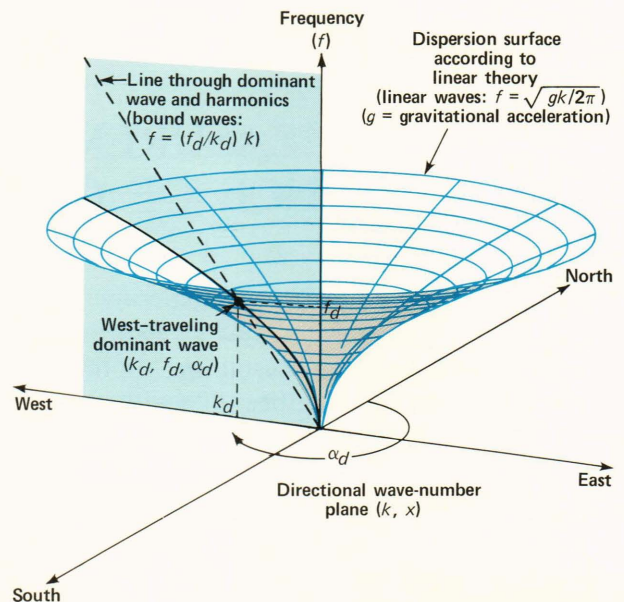

Figure 1 — Spectral domain for wave propagation dynamics. This example illustrates how bound and free waves can be distinguished through spectral analysis. The dominant wave, its harmonics, and free waves that are propagating west along the azimuth α_d have spectral representations lying in the plane outlined in blue. Spectral density of the dominant wave, characterized by wave number k_d and frequency f_d, and of its harmonics concentrates at points on the dashed red line. Free waves propagating along α_d are represented by spectral density along the solid red line. Free waves propagating in other directions will be represented by spectral density on other elements of the funnel-shaped surface of linear wave dispersion.

surements at a deep open-sea site. Subsequently, the data were processed at APL so that local maxima in the estimated spectra could be compared with wave propagation theory, which includes the advective frequency shift associated with the average measured current.

Two distinct, complementary systems measured the wave dynamics. Both were new designs intended to provide more complete spectrum estimates than had yet been reported. One system used an array of surface elevation transducers, the other a video camera. The array provides the more direct, and therefore the more easily interpreted, information on wave propagation. However, because it measures surface elevation at only 15 locations, its spatial resolution is low, and this limitation is a potential impediment to distinguishing free- from bound-wave spectral density, even when data-adaptive spectral estimation techniques are used. The proximity of the dashed and solid curves in Fig. 1 depicts this requirement for spectral resolution. The video system was designed to fill the requirement for high resolution. It is capable of acquiring wave images having 240 × 320 resolution elements (pixels) at a rate of 30 hertz, a very substantial increase over the spatial resolution of the array. The main drawback of the video technique is the dependence of its response (to surface slope rather than elevation) on sky radiance and re-

flection. This dependence causes the response of the video camera to be more variable and more nonlinear than that of the array. Thus, the two systems provide complementary data.

Stage I, a Navy research tower standing in 30 meters of water 18 kilometers off the coast of Panama City, Fla., was the site for the measurements. Figure 2a depicts the instrumentation layout. The array was mounted 6.6 meters from one leg of Stage I by means of the specialized supporting structure shown in Fig. 2b. A three-axis accelerometer package was mounted directly below the array to monitor the stability of the structure. Below the accelerometers at a nominal 4-meter depth, a two-axis electromagnetic meter measured water current in a horizontal plane. Above the array, wind speed and direction were monitored. A second, identical array was deployed on the opposite side of Stage I so that the dominant wave could always be measured before it passed under the tower, by using the appropriate array.

The array has 15 vertical wire transducers distributed horizontally to form a right angle. Spacings between the elements are 1.5 centimeters at the apex and increase by a factor of two with each additional transducer (with one exception: 25 centimeters was used instead of 24 centimeters) along either leg, so that the maximum spacing is 197.5 centimeters. Each transducer is a 3-meter-long, 1.5-millimeter-diameter insulated stainless steel wire that is pulled taut by a spring. The transducers are simply cylindrical capacitors for which seawater acts as the outer conductor. Waves moving past a transducer cause its capacitance to vary linearly with the wave profile. A unique electronic circuit measures the capacitance and converts it to voltage with better than 1% linearity.

The WAVDYN video system[6] utilized a modified RCA charge coupled device (CCD) camera, a video time-code generator, and a video recorder for data collection at the ocean site. The relation between sea-surface slope statistics and wave-image statistics is linear to a sufficient degree for the conditions of these measurements, as a number of theoretical and experimental efforts have shown.[7-9] The CCD camera monitored the waves propagating through its 13 × 25-meter field from the highest platform on Stage I. The depression angle was 30°, and an azimuth was chosen so that the dominant wave propagated nearly toward or away from the camera. That camera was complemented by another video camera that was aimed at the sky. Figure 2c depicts the cameras. The sky camera had a wide-field lens and provided images of the portion of the sky reflected into the CCD camera by the waves. Both cameras were equipped with red filters and horizontal polarizers to suppress their sensitivity to radiance upwelling from below the sea surface. Additional wind sensors were mounted above the cameras.

Data were recorded during a 6-day period beginning September 22, 1978. Typically, the wind was strongest (8 to 10 meters per second) during the morning and weakest (less than 5 meters per second)
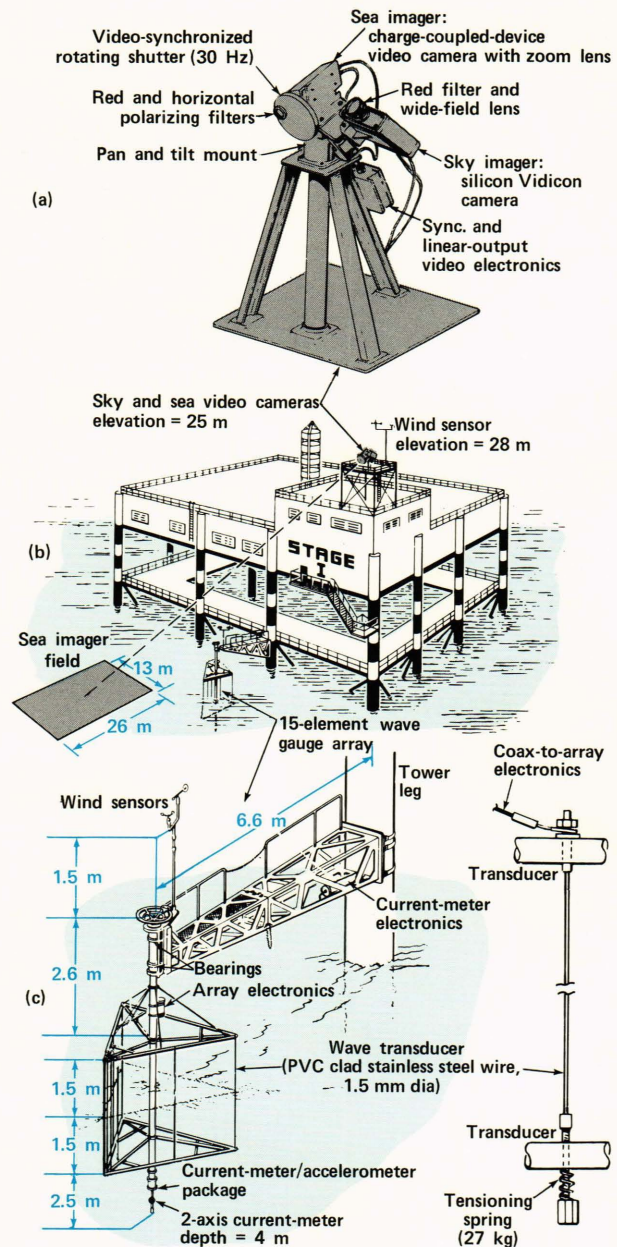

Figure 2 — WAVDYN instrumentation at Stage I, offshore Panama City, Fla.: (a) video cameras for wave imaging and sky imaging; (b) site layout; and (c) the wage gauge array structure.

during the afternoon. Figure 3 shows the wind and root-mean-square (rms) surface elevation histories at Stage I during the 6-day period. The vertical split lines denote intervals of data subjected to wave spectrum analysis. Data intervals are identified by a session number, that is listed above the upper scale in the figure. This number indicates when the data were acquired: the date in September 1978, morning (A) or afternoon (P), and a sequence number (I or II) if more than one session was conducted in the morning or the afternoon.
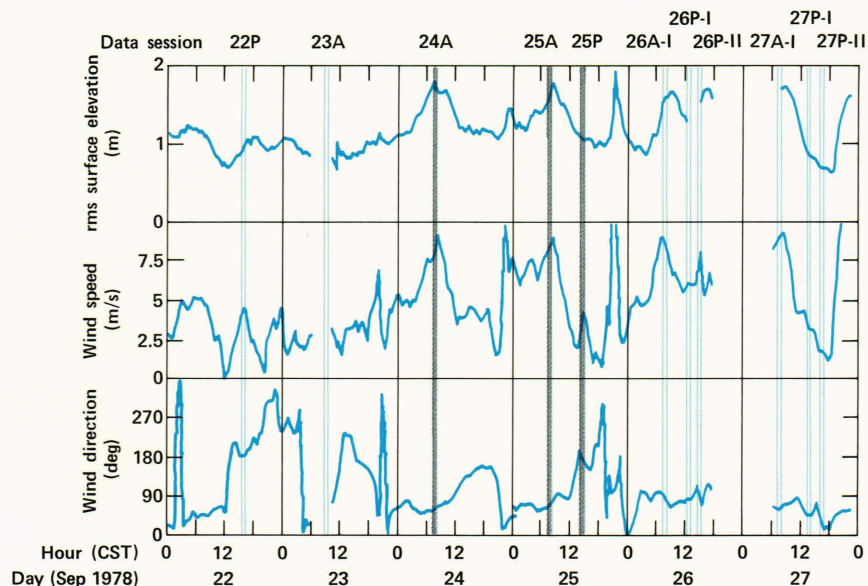
Figure 3 — Wind and rms surface-elevation histories during the WAVDYN measurements. The traces are interrupted by two intervals lacking data. The data-analysis intervals are noted as pairs of dashed vertical lines. They are called sessions and are identified by the code shown at the top of the plot.

DATA PROCESSING

Separate procedures were implemented for analyzing array and video data. This treatment was dictated by the difference in the sampling densities and in the data encoding (digital or analog). Figure 4 outlines the major steps in data acquisition and processing for the two systems.

Because the array data were recorded on computer-compatible tape at Stage I, sequences could be directly transferred from tape to APL's general-purpose (IBM 3033) computer system. This step also included demultiplexing the data stream and converting the values from digital to engineering units. In the temporal domain, the array data are not limited in terms of either sampling rate or sequence length; however, they are limited in both respects in the spatial domain. Therefore, standard fast Fourier transform (FFT) procedures work well for computing the temporal periodicity, whereas the maximum likelihood method (MLM) of spectral estimation is needed to enhance resolution in the spatial domain. For each selected 11-minute sequence of data, the result of this computation was an estimate of the directional wave-number/frequency spectrum of surface elevation variance.

The video data were analog-recorded on standard video cassettes together with a time code that identified each image. At APL, a dedicated system built around a PDP 11/34 minicomputer was used to extract image sequences for analysis, digitize them, and compute directional wave-number/frequency spectra using a three-dimensional FFT routine. The computer system uses standard components as peripherals but has special interfaces (designed and built at APL) between the video components and the computer and special software controlling the peripherals.

This video data processing system, with its software, is unique. Given instructions to digitize video

data beginning at a prescribed time and at a certain frame rate, the system reads the time code and locates the selected images in the analog data stream as the video cassette is played back on the video recorder. The image sequence is re-recorded on a video disk, where it is held for digitization. This intermediate analog storage slows the data rate (by repeatedly playing one frame for 20 seconds) to the level required by the video digitizer and the minicomputer. Digitized images are stored on a 260-megabyte disk. WAVDYN spectra estimation utilized 256-image sequences at 15 images per second; thus, the analysis interval spanned 17 seconds.

The transfer function between sea-surface slope and radiance typically causes the mean and the standard deviation of the radiance to increase from the near to the far field. Thus, a wave image is darker with less contrast in the near field. WAVDYN processing suppresses these trends. For detrending the mean, the signal from each pixel was reduced by its time-averaged level. Detrending the standard deviation required more effort. Standard deviation estimates are statistically less stable than mean estimates, so orthogonal, third-order polynomials were fitted to the set of estimates for an image sequence. Each image was then divided by the resulting polynomial function.

Two further adjustments to the video data were made before a spectrum was computed. Perspective distortion arising from the oblique imaging geometry was suppressed by ignoring displacements of the sea surface from the mean sea level and simply linearly interpolating between data to estimate signal levels over a regular grid of points in the sea level plane. The signal at the boundaries of the resulting image sequence was then tapered to zero. The three-dimensional spectrum was computed from the 256 × 256 × 256-element data set. Stability in this spectrum
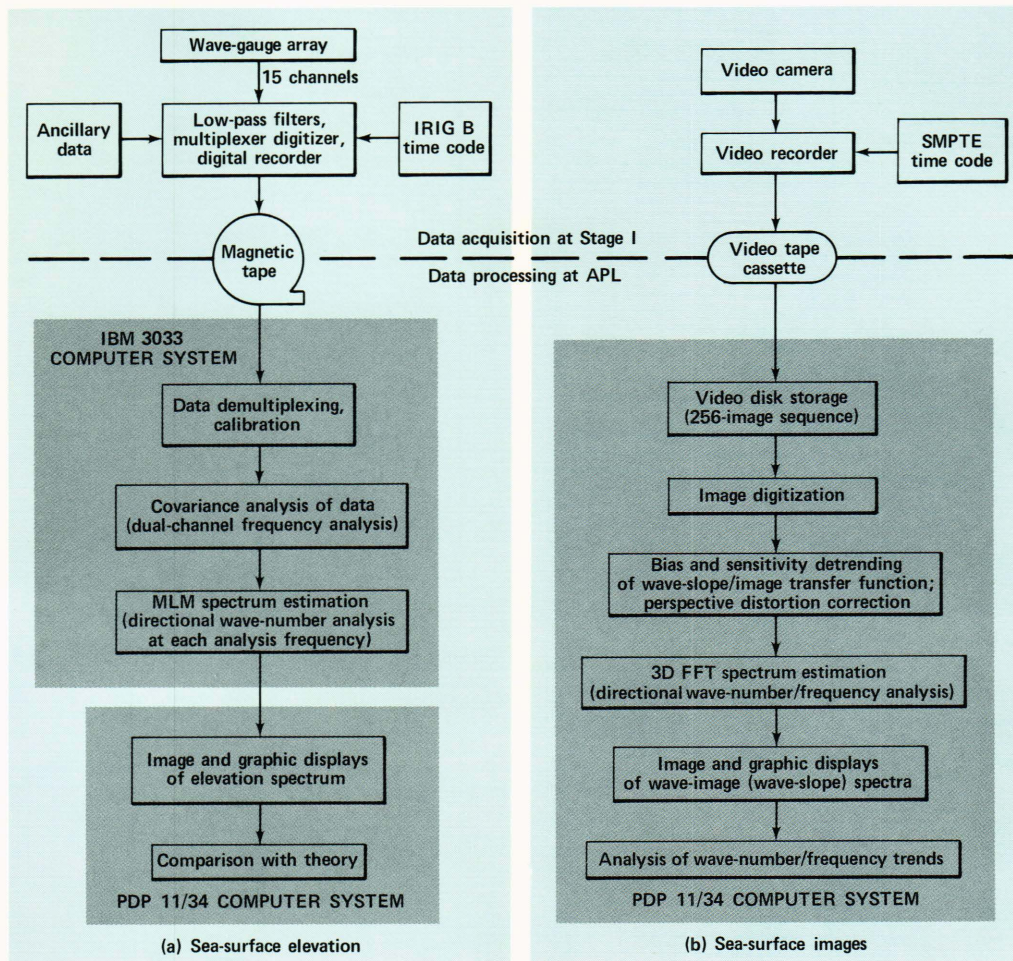
Figure 4 — Primary WAVDYN data acquisition and processing schemes: (a) sea-surface elevation; (b) sea-surface images.

was improved by smoothing with a $3 \times 3 \times 3$-point moving average.

ARRAY RESULTS

The spectra estimated from both the array and the video data are difficult to inspect because they are three-dimensional functions. Several procedures were implemented to display and to characterize them with reduced dimensionality. This article reports only some of these simplified forms. An understanding of their utility can be developed from their relationship to the directional wave-number/frequency spectral density of surface elevation, $G_{0a}(k, f, \alpha)$. Recall that k is the wavenumber, f is the frequency, and α is the wave propagation direction. Figure 5 shows two types of reduced spectra calculated from three different intervals of array data, each of which is identified by a session number. At the left are directional frequency spectra displayed on polar coordinates. The direction of wave propagation is the azimuthal coordinate; the frequency of a wave is the radial coordinate. The color-encoded, logarithmically scaled spectral density is

$$G_1(f,\alpha) = \int_0^\infty G_{0a}(k,f,\alpha)\,(k/f)\,dk , \qquad (1)$$

where the factor $1/f$ scales $G_{0a}(k, f, \alpha)$ correctly for the polar display. This reduced spectrum makes it easy to identify the frequency and direction of the dominant wave as the black dot in a white region.

At the right are azimuthal slices of $G_{0a}(k, f, \alpha)$ along the dominant wave direction α_d, like the plane outlined in blue in Fig. 1. The horizontal banding of this spectral density results from the poor spatial resolution of a sparse array. These conditional wave-number/frequency spectra, $G_{0a}(k, f; \alpha_d)$, are useful for comparing the location of spectral density structure relative to free- and bound-wave theories. The solid lines show the dispersion of free waves with infinitesimal amplitudes, taking into account frequency (Doppler) shifts caused by the measured current. Harmonics of the dominant wave lie on the dashed lines. These results show no clear bound-wave structure out to the third harmonic of the dominant wave. Such structure would appear as localized changes of color in the vicinity of integer multiples of k_d and f_d, which are denoted by tick marks inside the axes near the origin. Within the third harmonic, the spectral density follows the trend of linear theory. Beyond this frequency, experimental noise becomes a substantial contributor to the spectral structure, so it is
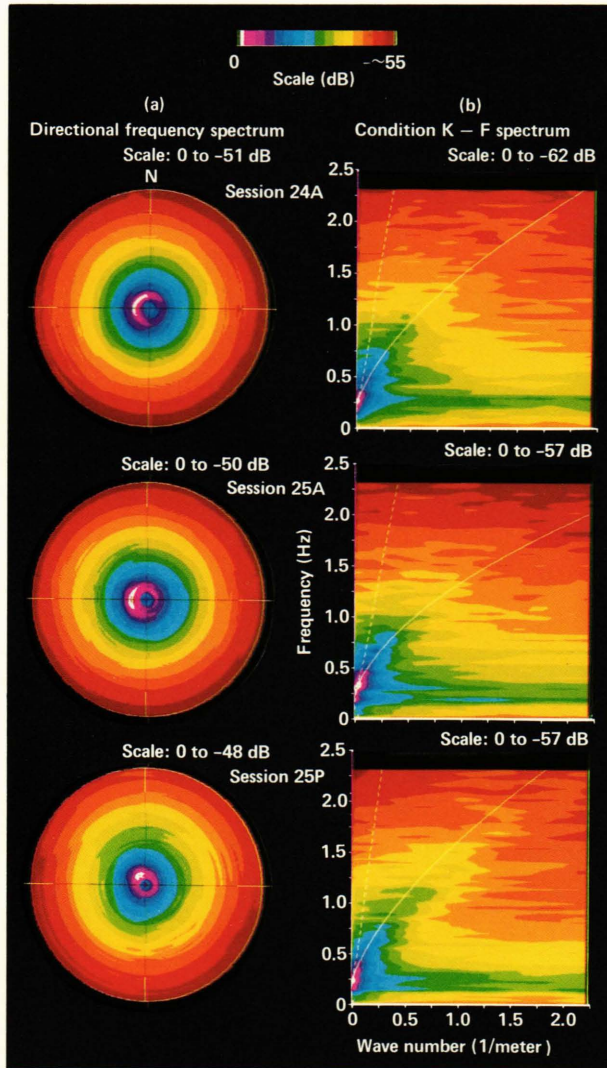
Figure 5 — Array-spectra color contours and comparison with theory. (a) Directional frequency spectra $G_1(f, \alpha)$. The radial coordinate is frequency, 0 to 2.31 hertz; the angular coordinate is direction, 0 to 360° with north up. (b) Conditional wave-number/frequency spectra $[G_{0a}(k, f; \alpha_d)]$ along the azimuth of the dominant local-wind wave. The solid line is linear theory; the dashed line locates the dominant wave and its harmonics.

Figure 6 — Bands for inspecting spectral density structure within ±30% of theoretical wave-number/frequency relationships.

Figure 7 — Distribution of frequency-averaged elevation spectral density about theoretical wave-number/frequency relationships. Shown are results from each interval of array data analyzed (see Fig. 3). The key information is the occurrence of spectral density maxima and their proximity to linear- and bound-wave theories, for which the normalized wave number equals 1.0 in the respective column.

difficult to draw justified conclusions regarding this region from these displays.

The utility of $G_{0a}(k, f; \alpha_d)$ is that it measures wave-like activity. Regions where it has locally high levels are important in this respect. The proximity of these regions to the theoretical wave-number/frequency relationships indicates whether bound or free waves better explain the spectrum. Consider two wave-number bands, like those in Fig. 6, extending 30% on either side of the wave numbers that the two theories associate with each frequency used for analyzing the data. The spectral density at each analysis frequency is normalized by dividing it by the maximum density at that frequency. This step enhances the lower density levels that occur at higher frequencies. Then, this normalized density is averaged over
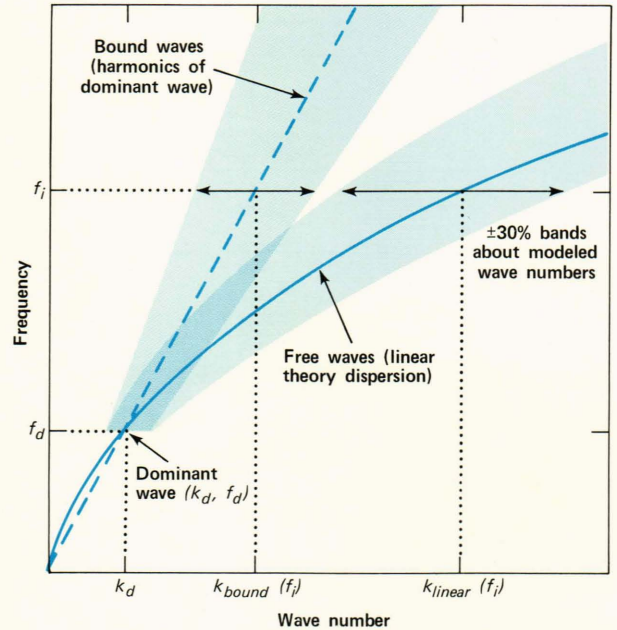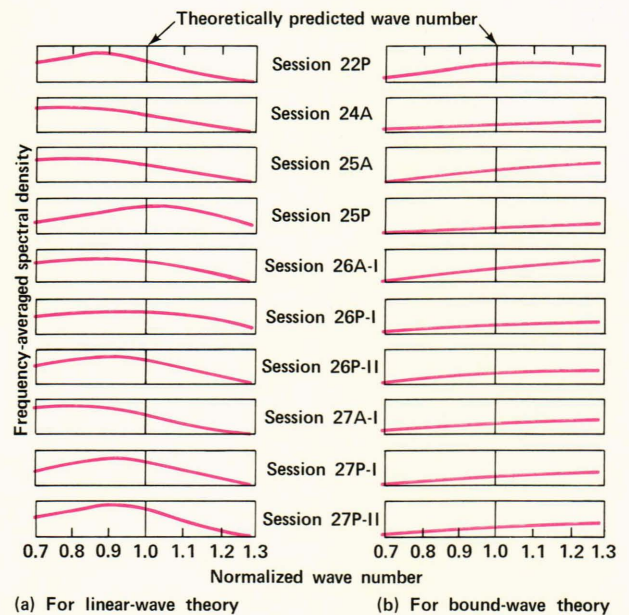
frequency at each of a set of normalized wave numbers that deviate from theory by prescribed percentages. The presence and location of a peak in the average density indicates the relative wave number at which the greatest wave-like activity occurred.

Figure 7 shows the results of such normalization and averaging applied to 10 different data sequences
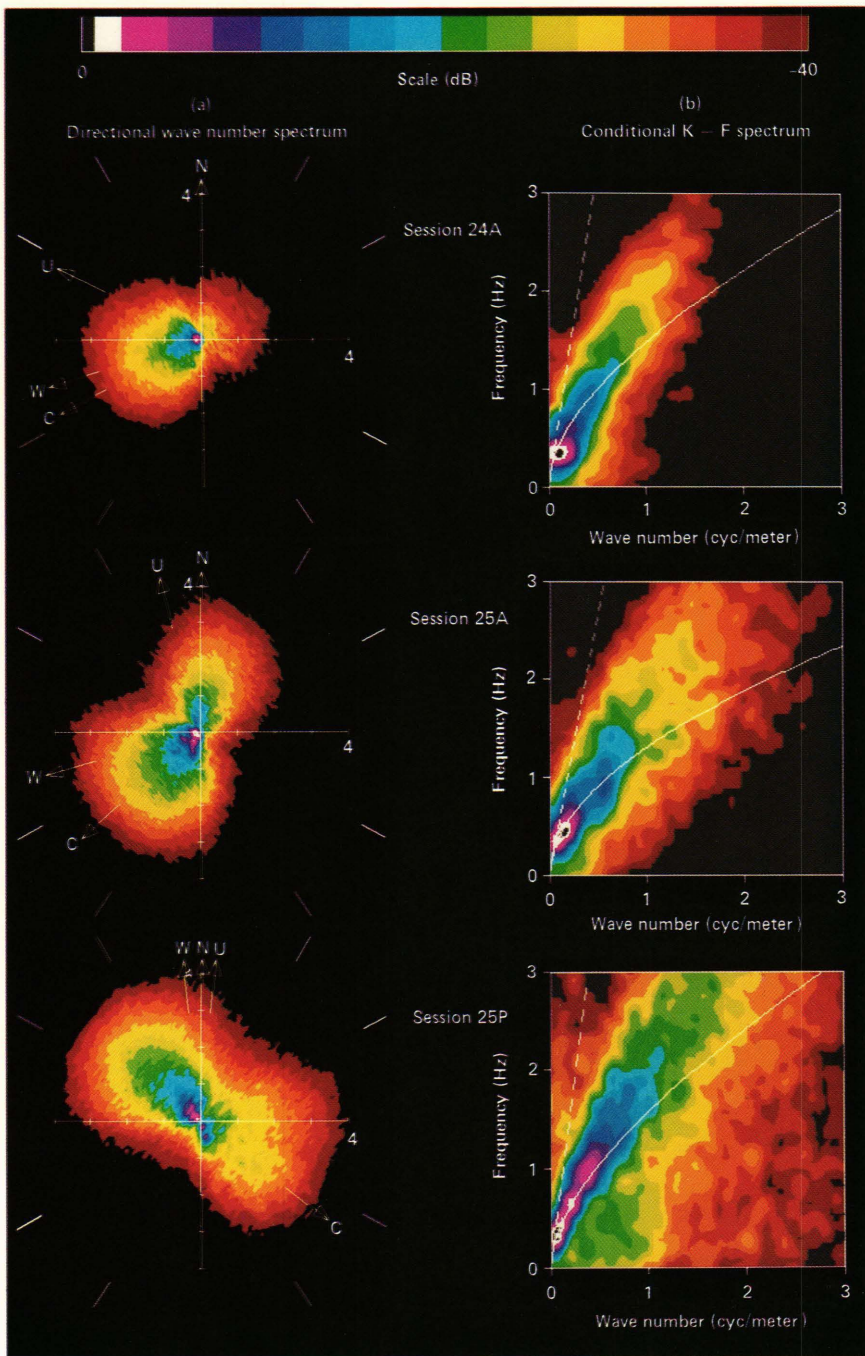
Figure 8 — Video-spectra color contours and comparison with theory. (a) Directional wave-number spectra, $G_2(k, \alpha)$. The radial coordinate is wave number, 0 to 4 cycles per meter; the angular coordinate is direction, 0 to 360° with N = north, W = wind vector, U = measured current, and C = camera azimuth. (b) Conditional wave-number/frequency spectra, $G_{0v}(k, f; \alpha_d)$, along the azimuth of the dominant local-wind wave. The solid line is linear theory; the dashed line locates the dominant wave and its harmonics.

spanning 6 days. The theoretically predicted wave number is 1.0 on these scales. Figure 7 provides information on the occurrence of distinct wave activity, which is indicated by a local maximum, and on the correspondence of such activity to either linear- or bound-wave theory, which is indicated by the proximity of a local maximum to the normalized wave-number value of 1.0 on the appropriate scale. The relative levels of the two curves for any of the sessions are not meaningful. These curves show that the prominent spectral structure for each sequence lies near and, with only one exception, below the normalized wave number for linear-wave theory. The

weakly nonlinear theory for free, finite-slope waves predicts similar behavior, albeit with a smaller offset from the linear theory curve. There are no well-defined peaks in the region of the normalized wave number predicted by bound-wave theory.

VIDEO RESULTS

Spectra from the video data provide information similar to that from the array. Two spectral forms derived from the directional wave-number/frequency spectra of video data, $G_{0v}(k, f, \alpha)$, are shown in Fig. 8. The spectral density is logarithmically scaled and color encoded as indicated by the color bar.

At the left are directional wave-number spectra. Wave-number is the radial coordinate; wave direction is the angular coordinate. This spectral form is related to the three-dimensional spectrum through an integral:

$$G_2(k,\alpha) = \int_0^\infty G_{0v}(k,f,\alpha)\, df. \qquad (2)$$

Similar to the directional frequency spectra from the array, these spectra are convenient for visualizing average wave activity. However, there are two important differences. First, wave slope is the key property of the surface that causes modulation in an image since both the reflection coefficient and the reflected region of the sky vary with slope. Thus, in the absence of other effects, the ratio of video to array spectral density should vary as k^2, because slope is the derivative of elevation and the spectrum represents slope squared. This relationship means that the video spectra do not roll off with wave-number or frequency as rapidly as do the array spectra. Second, the transfer function between slope and radiance varies with the direction of wave propagation. The transfer function is generally greater for waves propagating toward or away from the camera, but clouds can significantly distort this azimuthal trend.

Appearing at the right in Fig. 8 are conditional wave-number/frequency spectra, $G_{0v}(k, f; \alpha_d)$, corresponding to the dominant wave azimuth resolved by the array. Again, the solid line indicates linear

wave-theory dispersion, while the dashed line locates harmonics of the dominant wave. Advection by the measured current is included in these theoretical relations. These and similar spectra for other analysis intervals identify no predominant bound-wave activity. The spectra agree generally with free-wave theory, although in every case the trend of the structure is higher in frequency than predicted by linear theory *for azimuths aligned with the dominant wave*. These observations are more evident here than in the array spectra because the spatial resolution is higher and the spectral density is more structured over the regions where the theoretical relations are well separated. The breadth of the spectral trends is largely the manifestation of frequency and wave-number modulations of short waves caused by the orbital flow of the dominant wave.

These spectra also indicate the presence of steady advection in addition to that produced by the measured current: the spectral structures deviate further above the linear theory curve with increasing wave number and frequency. The possibility of an additional current affecting waves shorter than the dominant wave is strongly suggested by the spectra of Fig. 9. Here, the 12 conditional wave-number/frequency spectra surrounding the directional wave-number spectrum correspond to the 12 directions of wave propagation indicated by the radial lines. North is up. As the wave propagation direction varies, the spectral density trend changes its position sinusoidally relative to the linear-theory curve.
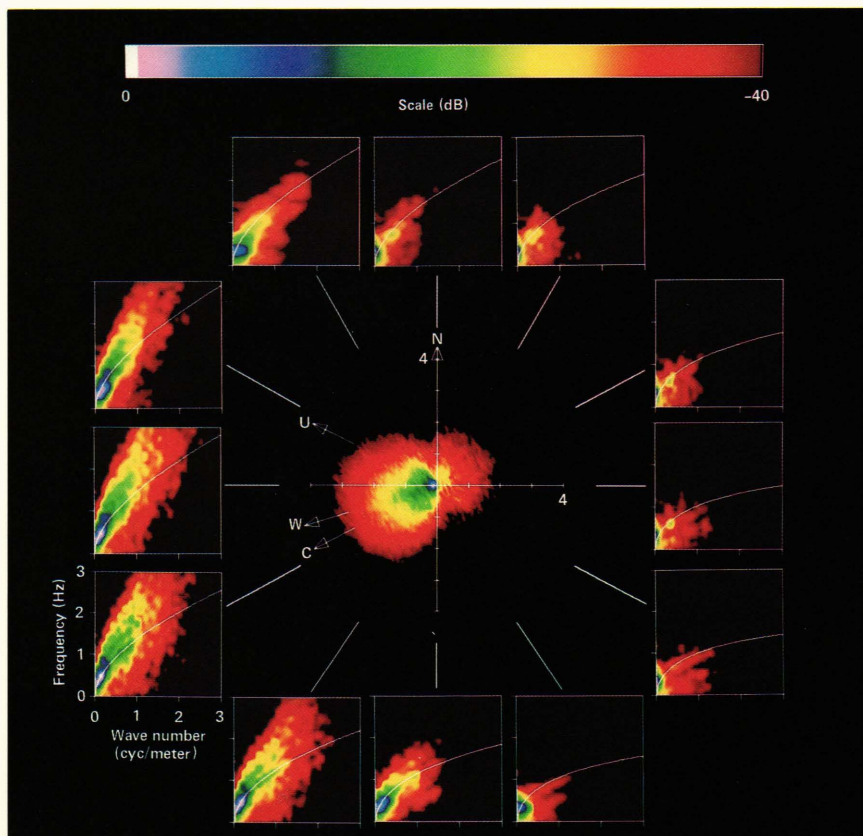

Figure 9 — Video conditional wave-number/frequency spectra encompassing the directional wave-number spectrum, Session 25P.

The puzzling aspect of this observation is how a current could have affected wave propagation, particularly the short waves, yet not have been resolved by the current meter. There are at least two possibilities: the wind-drift current and the orbital current of the dominant wave.

The stress of wind blowing over a water surface creates a vertically sheared current very near the surface. Under light-to-moderate winds, like those during WAVDYN, the wind-drift current is negligible at 4-meter depths. Thus, short waves are advected more by that current than long waves because more of their particle motion is confined to the shallow depths of the current. Furthermore, at the surface, the wind-drift current is only 3 to 5% of the wind speed which is not enough to account for all of the observed discrepancy.

The second possibility, advection by the orbital flow of the long waves, is a large enough effect provided the short waves are steepened near the crests and flattened near the troughs of the long waves. At the crest, orbital flow is maximum in the direction of wave propagation. Thus, the steeper short waves near the long-wave crests would dominate the spectrum at high wave numbers. Their frequencies would appear higher when they are traveling with the long waves and lower when they are traveling against the long waves. Four-minute averaging was used to process the current data in order to exclude the oscillatory flow of the waves from the measured current. Thus, this second possibility is not taken into account in the dispersion curves that are shown in Figs. 5, 7, 8, 9, and 10.

In spectra from six of the eight wave-image sequences that were processed, the magnitudes and directions of the additional current are resolved. Values for these parameters were calculated by a technique that finds the current vector that best superimposes linear wave theory on the frequency centroids of the conditional wave-number/frequency spectra taken at 30° increments, such as those in Fig. 9. Figure 10 exemplifies this fitting procedure. At the left is a set of points representing the deviation of the phase speed along a single azimuth. A point for each analysis wave number was determined by using the frequency centroid of the spectral density and linear wave theory, which includes advection by the measured current. At the right are *average* phase-speed deviations determined at 30° intervals of analysis azimuth. The average was computed over a wave-number range that varied with analysis azimuth so that regions where the spectral density is corrupted by noise were rejected. The average phase-speed deviations of six of the eight intervals of video data analyzed are well characterized by a cosine dependence on azimuth, such as the curve drawn through the data in Fig. 10b. Table 1 lists the results of this analysis along with estimated wind-drift currents and currents at the crests of the long waves. These crest currents were computed by assuming that the measured rms elevation arises solely from a sinusoidal wave having the dominant-wave frequency. This is a gross simplification but useful for estimating the upper bound of this effect. Table 1 demonstrates that wind-drift current cannot alone account for the deviation between linear theory and the video spectra, whereas differential steepening and advection of short waves caused

Table 1

COMPARISON OF ADDITIONAL CURRENT DEDUCED FROM VIDEO SPECTRA WITH WIND-DRIFT CURRENT AND WITH DOMINANT-WAVE CREST CURRENT

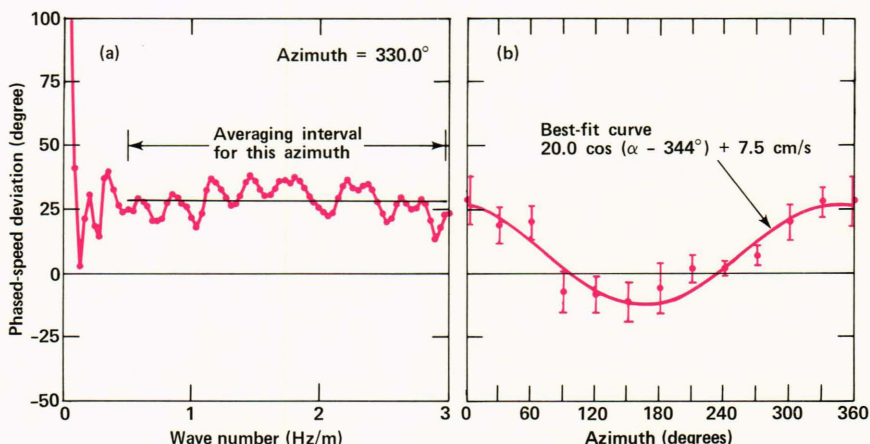| Session	Additional Current (cm/s)	Wind-Drift Current (cm/s)	Current at Crest of Dominant Wave (cm/s)
22P	33	8	38
23A	10	10	16
24A	40	18	34
25A	28	16	39
25P	20	5	15
26P-II	17	11	35

Figure 10 — Deviation of the video-derived phase speed from linear theory adjusted for measured current, Session 25P. (a) Deviation as a function of wave number along the azimuth of the dominant wave. The dotted line denotes the wave-number range over which the deviation was averaged to determine the datum at 330° in (b). (b) Average deviation as a function of azimuth. The rms error bars and the best-fit cosine curve are shown.

by the dominant wave can explain much of the deviation. Apparently, short-wave straining is an important effect and should be taken into account when making high-frequency wave measurements.

SUMMARY AND CONCLUSIONS

WAVDYN has substantially improved the empirical basis for developing explanations of how components of ocean wind-wave spectra propagate and interact. Requisite for this endeavor was the implementation of modern techniques for resolving wave statistics with greater detail than was previously achieved and for displaying them in a number of forms. These techniques included two key systems: a wave-gauge array system and a wave-imaging system. The array system, with digital data recording and processing, measured surface elevation variations and computed directional wave-number/frequency elevation spectra by the maximum likelihood method. It also provided measurements of the average currents that advected the waves. The imaging system used a CCD video camera with a video recorder to acquire sequences of wave images from which directional wave-number/frequency spectra of surface slope were estimated by using specialized processing software, including a three-dimensional FFT. These two systems are developed to a functional level.

Results from WAVDYN represent wave characteristics during light-to-moderate winds (≤ 10 meters per second) and for both building and decaying seas. Ten intervals of array data and eight intervals of video data, acquired over a period of six days, were processed. In contrast to some laboratory measurements, none of the results shows that nonlinearity prevails over the free waves generated from turbulent processes. The video data especially bore out this conclusion because they have better spatial resolution than array results and greater sensitivity at high wave numbers and frequencies where bound and free waves have greater spectral separation. At high wave numbers, the video spectra show an effect similar to advection but not attributable to the measured average current. Rough estimates indicate that this effect can be explained as differential roughening of the short waves near the crests of the dominant wave, where its orbital current is greatest and aligned with its propagation direction.

REFERENCES

[1] B. L. Gotwols and G. B. Irani, "Optical Measurement of the Phase Velocity of Ocean Waves During the 1978 Wave Dynamics Experiment," *Johns Hopkins APL Tech. Dig.* **2**, 56-62 (1981).
[2] B. M. Lake and H. C. Yuen, "A New Model for Nonlinear Wind Waves. Part 1. Physical Model and Experimental Evidence," *J. Fluid Mech.* **88**, 33-62 (1978).
[3] A. Ramamonjiarisoa and M. Coantic, "Loi Experimentale de Dispersion des Vagues Produites par le Vent sur Une Faible Longueur d'Action," *C. R. Acad. Sci. Paris, Ser. B*, 111-113 (1976).
[4] A. Ramamonjiarisoa and J. P. Giovanangeli, "Observations de la Vitesse de Propagation des Vagues Engendrées par le Vent au Large," *C. R. Acad. Sc. Paris, Ser. B*, 133-136 (1978).
[5] H. C. Yuen and B. M. Lake, "Nonlinear Wave Concepts Applied to Deep Water Waves," in *Solitons in Action*, Academic Press, New York, pp. 89-126 (1978).
[6] B. L. Gotwols and G. B. Irani, "A CCD Camera System for Remotely Measuring the Dynamics of Ocean Waves," *Appl. Opt.* **21**, 851-860 (1982).
[7] R. D. Chapman and G. B. Irani, "Errors in Estimating Slope Spectra from Wave Images," *Appl. Opt.* **20**, 3645-3652 (1981).
[8] F. M. Monaldo and R. S. Kasevich, "Daylight Imagery of Ocean Surface Waves for Wave Spectra," *J. Phys. Oceanogr.* **11**, 272-283 (1981).
[9] D. Stilwell and R. O. Pilon, "Directional Spectra of Surface Waves from Photographs," *J. Geophys. Res.* **79**, 1277-1284 (1974).